SUSHI: Sparsity-Based Ultrasound Super-Resolution Hemodynamic Imaging

Avinoam Bar-Zion, Oren Solomon, *Student Member, IEEE*, Charles Tremblay-Darveau, Dan Adam, *Member, IEEE*, and Yonina C. Eldar, *Fellow, IEEE*

***Abstract*— Identifying and visualizing vasculature within organs and tumors has major implications in managing cardiovascular diseases and cancer. Contrast-enhanced ultrasound scans detect slow-flowing blood, facilitating noninvasive perfusion measurements. However, their limited spatial resolution prevents the depiction of microvascular structures. Recently, super-localization ultrasonography techniques have surpassed this limit. However, they require long acquisition times of several minutes, preventing the detection of hemodynamic changes. We present a fast super-resolution method that exploits sparsity in the underlying vasculature and statistical independence within the measured signals. Similar to super-localization techniques, this approach improves the spatial resolution by up to an order of magnitude compared to standard scans. Unlike super-localization methods, it requires acquisition times of only tens of milliseconds. We demonstrate a temporal resolution of ∼25 Hz, which may enable functional super-resolution imaging deep within the tissue, surpassing the temporal resolution limitations of current super-resolution methods, e.g., in neural imaging. The subsecond acquisitions make our approach robust to motion artifacts, simplifying *in vivo* use of super-resolution ultrasound.**

***Index Terms*— Compressed sensing (CS), contrast-enhanced ultrasound (CEUS), sparse representation, super-localization microscopy, super-resolution, super-resolution optical fluctuation imaging.**

I. Introduction

ULTRASOUND (US) is a cost-effective, reliable, noninvasive, and radiation-free imaging technique. The use of encapsulated gas microbubbles as contrast agents extends the capabilities of US to the imaging of fine vessels with low flow velocities. Specifically, contrast-enhanced US (CEUS) enables real-time hemodynamic and perfusion imaging with high-penetration depth. However, like many noninvasive imaging modalities, spatial resolution limitations prevent classic CEUS imaging from resolving the fine structure of the microvasculature. Therefore, despite their superior penetration depth, classic US measurements are limited in their capability to detect microvascular changes in response to anticancer [1] and anti-inflammatory treatment [2], and produce functional maps with limited spatial resolution, compared to optical scans [3], [4]. Since anticancer and anti-inflammatory treatments are known to cause structural changes in the microvascular level [5], resolving these vessels could enable fast and direct treatment monitoring capability, valuable for both research and clinical applications. Furthermore, when neural activity is increased, most of the blood flow enhancement is performed in the capillaries [3], so that functional imaging at this level may enable better understanding of neural activity.

Several CEUS super-localization techniques that were introduced in the last few years, were shown to surpass the classic resolution limitations dictated by the point spread function (PSF) of the US system and provide subdiffraction scans [6]–[12]. Inspired by optical fluorescent microscopy methods like PALM [13] and STORM [14], these techniques overcome the diffraction limit by capturing a series of frames, each composed of a sparse distribution of microbubbles. The main assumption in these methods is that the microbubbles in each frame are resolvable, and therefore the center of each echo is estimated with subdiffraction resolution. By applying a super-localization procedure and accumulating the localizations over many frames, the overall structure of interest can be revealed. In CEUS super-localization, the assumption of sparse microbubble distribution is satisfied by using very low concentrations of microbubbles [7], [8], [12]; bursting subpopulations of microbubbles [9]; and filtering with spatiotemporal filters to capture subsets of microbubbles [6]. By estimating the centers of resolvable PSFs, an improvement of up to tenfold in spatial resolution was reported [6]. Super-localization has found a range of preclinical applications including 3-D anatomical imaging of vessels in the brain [6] and in tumors [10].

Despite recent advances in CEUS super-localization, these methods are still limited by low temporal resolution (typically tens to hundreds of seconds) and large amounts of data (tens of thousands of sequential images) that need to be stored and processed [6], [8]. Reducing these long acquisition times and limiting CEUS super-resolution scans to less than a second is important for two main reasons. First, fast hemodynamic changes, with a timespan of a few seconds and less [15], cannot be captured by current super-localization methods. Therefore, these techniques do not have the temporal resolution needed for functional imaging applications such as functional US imaging of the brain. Second, long acquisition times make super-localization sensitive to motion artifacts.

Manuscript received May 4, 2018; accepted September 25, 2018. Date of publication October 2, 2018; date of current version December 20, 2018. This work was supported by the European Union's Horizon 2020 research and innovation program under Grant 646804-ERC-COG-BNYQ. *(Avinoam Bar-Zion and Oren Solomon contributed equally to this work.) (Corresponding author: Avinoam Bar-Zion.)*

A. Bar-Zion and D. Adam are with the Department of Biomedical Engineering, Technion-Israel Institute of Technology, Haifa 32000, Israel (e-mail: barz@campus.technion.ac.il; dan@biomed.technion.ac.il).

O. Solomon and Y. C. Eldar are with the Department of Electrical Engineering, Israel Institute of Technology, Haifa 32000, Israel (e-mail: orensol@campus.technion.ac.il; yonina@ee.technion.ac.il).

C. Tremblay-Darveau is with the Department of Medical Biophysics, University of Toronto, Toronto, ON M5G1L7, Canada (e-mail: charles.tremblay.darveau@mail.utoronto.ca).

Digital Object Identifier 10.1109/TUFFC.2018.2873380

These artifacts are difficult to compensate for in postprocessing since the motion is 3-D and CEUS imaging is commonly performed in 2-D [1]. In addition, breath holds have limited efficiency since many patients cannot hold their breaths for long periods of time [16]. Consequently, long acquisition times limit the clinical applicability of CEUS super-localization, especially when imaging internal organs whose scans are highly affected by motion artifacts [17].

Inspired by an optical fluorescence microscopy method named SOFI [18], an alternative approach for improving spatial resolution in CEUS imaging was recently presented [19], termed CEUS SOFI. Relying on the independence of fluctuating CEUS signals in neighboring vessels, high-order statistics of the time-series measured in each pixel are estimated. This technique was shown to produce improvement in spatial resolution that scales with the order of the statistics. Avoiding the assumption of resolvable microbubbles, high US contrast agents' concentrations were used, enabling short acquisition times and high temporal resolution. However, in practice, the order of the statistics used in SOFI is limited by both the signal-to-noise ratio (SNR) and dynamic range of CEUS signals, restricting the typical resolution improvement to a factor of 2.

Here, we present an approach for fast CEUS super-resolution, termed sparsity-based US super-resolution hemodynamic imaging (SUSHI), which extends the preliminary results presented in [20]. The main goal of SUSHI is fast detection and depiction of hemodynamic changes with sub-diffraction resolution. To this end, SUSHI uses high UCA concentration to maximize the portion of the vasculature imaged during ultrafast acquisitions and makes use of the statistical independence between the fluctuations of CEUS signals originating from different vessels. In addition, SUSHI exploits the sparsity of the underlying vascular structure to improve the spatial resolution beyond the diffraction limit, by relying on sparse recovery techniques [21]–[24].

Super-resolution imaging by exploiting sparsity in the correlation domain was recently introduced in the context of fluorescence microscopy, in a method called sparsity-based super resolution correlation microscopy (SPARCOM) [25], [26]. SUSHI extends the ideas of SPARCOM to CEUS imaging by exploiting sparsity within the CEUS correlation domain. However, the signal model in CEUS imaging differs from its optics counterpart, as statistical independence between UCA signals can only be assumed between different blood vessels. Moreover, the CEUS signal includes phase measurements, unlike fluorescent signals which contain magnitude only. SUSHI exploits the phase of the received signal to separate between vessels with opposite flow via Doppler processing, prior to performing sparse recovery. This separation provides additional anatomical information, based on flow directions, and results in sparser signals for both arteries and veins, compared with the original non-Doppler filtered signal. Sparse recovery in the correlation domain allows SUSHI to reduce acquisition time dramatically and operate with short, subsecond acquisition rates and high UCA concentrations, while achieving spatial resolution close to that of super-localization techniques.

In recent years, sparse representations of signals [27], [28] and the theory of compressed sensing (CS) [23], [24] have gained popularity and found applications in many research fields such as radar [29], magnetic resonance imaging (MRI) [30], and US imaging [31]. A discrete signal is said to be sparse, if it can be represented as a linear combination of a small number of functions. That is, in an appropriate transform domain, the signal can be represented by a vector with most coefficients zero, except a small number of nonzero values at unknown locations. CS techniques aim at estimating the locations and values of these coefficients. The theory underlying CS asserts that such a sparse vector can be recovered exactly from a small number of linear measurements taken in a nonadaptive manner [27]. CS has also been used to enable super-resolution in fields such as fluorescence microscopy [25], and coherent diffraction imaging [32], to name a few. In addition, recent works [33], [34] have shown that sparse recovery in the correlation domain may lead to a dramatic increase in the number of detected sources, compared with sparse recovery performed on the signal itself.

The rest of the paper is organized as follows. A parametric model for CEUS signals, including Doppler information, is presented in Section II. Based on this model, statistical independence in CEUS signals is discussed in Section III. SUSHI processing that uses this statistical independence together with sparsity in the underlying vascular structures is described in Section IV. In Sections V and VI, we show improvement in spatial resolution comparable to super-localization, but with much higher temporal resolution. Our results are analyzed and discussed in Section VII. Section VIII concludes this paper.

Throughout this paper, x represents a scalar, $\boldsymbol{x}$ a vector, and $\boldsymbol{X}$ a matrix. The size of a matrix $\boldsymbol{A}$ is denoted by $M \times N$, such that $\boldsymbol{A}$ has M rows and N columns. The kth discrete Fourier transform coefficient of $x[p]$, $p = 1, \ldots, P$ is denoted using capital letters and index k, $X[k], k = 1, \ldots, P$. The notation $||\cdot||_p$ indicates the p-norm. Square brackets $[\cdot]$ relate to discrete-time signals, while round brackets $(\cdot)$ indicate continuous-time signals.

II. CEUS Signal Model and Doppler Processing

In this section, we specify the analytical model we assume to describe the acquired CEUS signal. This model is then used for Doppler processing, which is a preprocessing step in the overall SUSHI algorithm. It also enables us to exploit the inherent sparsity within the signal to achieve super-resolution, as we describe in Section IV.

A. Signal Model

CEUS imaging is performed by transmitting a series of US pulses toward the region of interest with uniform time differences ΔT. This series of P measurements is performed over an interval $t \in [0, T]$, where $T = P\Delta T$. The received signals in the transducer elements are focused upon reception in a process called beamforming to produce an US map of the interrogated tissue and are then demodulated to produce the IQ signal. The IQ signal f is composed of the desired blood signal b, resulting from echoes of individual microbubbles,

and contaminated by the tissue clutter c and an additive noise component w [35]

$$f(x,z,t) = c(x,z,t) + b(x,z,t) + w(x,z,t). \quad (1)$$

Here, x and z are the lateral and axial coordinates, respectively. Our goal is to utilize the acquired microbubbles signal b to achieve a subdiffraction representation of the underlying vasculature, with subsecond acquisition times. The first step in our processing scheme is to estimate the relevant blood related component b from f. We then exploit the inherent sparse structure of the underlying vasculature, described in Section IV, to achieve fast, super-resolved CEUS imaging.

The removal of clutter noise from CEUS data and the estimation of b, denoted as $\hat{b}$, is usually performed based on two priors: the nonlinear (harmonic) nature of the echoes produced by the microbubbles at low acoustic pressure, and their distinct velocity patterns. Pulse sequences containing several pulses with different amplitudes and/or phases were developed to separate the nonlinear signal component [36]. The echoes resulting from these different pulses are weighted and combined as a preliminary processing step. Next, temporal [37] or spatiotemporal [35] filters can be used to remove the remaining nonlinear clutter noise and produce an estimation of the blood related signal $\hat{b}$. IIR filters with projection initialization [37] were used in this work since this method's cutoff parameter is directly connected to the minimal flow velocity in the estimated blood signal and therefore is easier to interpret and control.

We now turn to describe an analytical model for $\hat{b}$, which will enable us to perform additional Doppler processing and to formulate the SUSHI processing. We assume that the US acquisition is performed by a linear, shift invariant system. Therefore, at any given time, the filtered blood related signal $\hat{b}$ can be written as a convolution between the reflectivity function of the scanned object, denoted by $i(x,z,t)$, and the PSF of the system $h(x,z)$. Denoting the time-dependent set of detected bubbles at time t as K(t), the reflectivity of the UCAs, $i(x,z,t)$, is modeled as a sum of Dirac delta functions $\delta(\cdot,\cdot)$ at time-varying positions $(x_q(t), z_q(t))$, such that

$$i(x,z,t) = \sum_{q\in K(t)} \delta(x - x_q(t), z - z_q(t))\sigma_q \quad (2)$$

where σ_q represents the scattering of each bubble. A physical model for the echo from a single bubble can be found in [38]. Signal $\hat{b}$ is the convolution between $i(x,z,t)$, defined in (2), and the PSF, resulting in a stream of pulses model [19]

$$\hat{b}(x,z,t) = \sum_{q\in K(t)} h(x - x_q(t), z - z_q(t))\sigma_q. \quad (3)$$

This stream-of-pulses model for CEUS signals is similar to the one in [39].

By discretizing the positions of the microbubbles in (3) and associating them with one of N_p neighboring volume cells in which they are located at a given time, $\hat{b}$ can be described by the following equation [19]:

$$\hat{b}[m\Delta_{xL}, l\Delta_{zL}, t] \approx \sum_{n=1}^{N_P} h[m\Delta_{xL} - x_n, l\Delta_{zL} - z_n]s_n(t) \quad (4)$$

where $m,l \in \{1,\ldots,M\}$ and $[\Delta_{xL}, \Delta_{zL}]$ are the indices and dimensions of the pixels in the beamformed image, respectively, (L stands for "low," as in the low-resolution beamformed image); $[x_n, z_n]$ are the positions of the N_p microbubble-containing pixels; and $s_n(t)$ is the time dependent signal, summing the contributions σ_q of all the bubbles in each bubble-containing pixel. Here, we consider a square image for convenience only, although the method is easily applicable to rectangular images.

The time-dependent fluctuations in each pixel $s_n(t)$ include a multiplicative envelope a and a complex phase whose temporal change over consecutive acquisitions is affected by the velocity of the moving contrast agents. In US imaging, we measure $s_n(t)$ at $t = p\Delta T$, where p is the transmitted pulse index. Following [40] and the derivation in [41] for a single scatterer, $s_n[p\Delta T]$ is described as:

$$s_n[p\Delta T] = a[p\Delta T] \sum_{u\in U_n} \exp^{-j\nu_u p\Delta T + \beta_0}. \quad (5)$$

The set U_n contains the microbubble velocities detected within each volume cell n during the imaging interval, ν_u are their Doppler angular frequencies, and β_0 is a random constant phase. Each Doppler angular frequency is related to a specific axial velocity $v_{z,u}$, by the following relation:

$$\nu_u \equiv 2\pi(2f_0 v_{z,u}/c). \quad (6)$$

Here, c is the velocity of sound in the medium and f_0 is the center frequency of the US wave. A single volume cell n can contain bubbles belonging to several vessels or streamlines with different Doppler angular frequencies ν_u. In previous works, the random envelop a was shown to follow the K-distribution [42].

The complex phase in (5) enables the use of Doppler processing, not only to remove clutter noise but also to decompose the CEUS signal according to the blood flow velocities within the vessels. By doing so, CEUS signals that belong to different blood vessels with distinct Doppler signals can be separated even if they spatially overlap. This Doppler processing is performed on each pixel's time-trace separately.

B. Doppler Processing

Next, we detail our Doppler preprocessing, starting with a single pixel, whose time trace is given by (4), sampled at times $t = p\Delta T$. In the following, the ΔT notation is removed, for convenience. Considering (4) at discrete time points p, we obtain the P-point temporal discrete Fourier transform (DFT) of $\hat{b}$ in pixel $[m,l]$ as

$$B_{m,l}[k] = \mathrm{DFT}\left\{\sum_{n=1}^{N_P} h[m\Delta_{xL} - x_n, l\Delta_{zL} - z_n]s_n[p]\right\}$$
$$= \sum_{n=1}^{N_P}\sum_{u\in U_n} h[m\Delta_{xL} - x_n, l\Delta_{zL} - z_n]A_u[k] \quad (7)$$

where the DFT of the uth velocity component from (5) ($\mathrm{DFT}\{s_n[p]\}$) is given by

$$A_u[k] = \mathrm{DFT}\{a[p]e^{-j\nu_u p\Delta T + \beta_0}\}[k], \quad k = 0,\ldots,P-1. \quad (8)$$

The double sum in (7) presents the contribution of the velocity distribution U_n in each bubble-containing location n. As part of our Doppler processing we divide the continuous Doppler spectrum of the imaged blood vessels into U bands. By doing so and looking at the entire scan instead of a single pixel, we can reorder the double sum in (7) according to a desired number of bands U, and the number of volume cells containing microbubbles in each Doppler band N_u. Subsequently, the signal $B_{m,l}[k]$ is decomposed according to its spectral content

$$B_{m,l}[k] = \sum_{u=1}^{U} \left(A_u[k] \sum_{n \in N_u} h[m\Delta_{xL} - x_n, l\Delta_{zL} - z_n] \right). \quad (9)$$

Since we divide $B_{m,l}[k]$ into U different Doppler bands (which together cover the entire spectrum), we may apply a series of temporal bandpass filters to the time series in each pixel, to separate the bands. By doing so, the blood signal $\hat{b}$ at pixel $[m, l]$ is decomposed into D_f signals, each denoted by $\hat{b}^d$, with different flow characteristics

$$\hat{b}^d_{m,l}[p] = \mathrm{DFT}^{-1}\left\{ B_{m,l}[k] \Pi^d_{m,l}[k] \right\}[p], \quad (10)$$

where $\Pi^d, d = 1, \ldots, D_f$ correspond to the series of D_f temporal bandpass filters that together cover the relevant Doppler frequency bands. These temporal filters are applied to each pixel's time-trace, in parallel. When applied to all the pixels in the scan, this Doppler processing results in D_f movies, each showing different flow patterns and sparser vasculature, divided according to the different Doppler velocities. In this work, we chose $D_f = 2$, and used one filter to separate the positive frequencies and another to separate negative frequencies, with respect to the transducer. Thus, arterial and venous vasculature could be separated (as presented in Fig. 2), according to the direction of flow. An illustration of the temporal filters is given in Fig. 5.

In the time domain, the filtered signal $\hat{b}^d$ in (10) is given by

$$\hat{b}^d[m\Delta_{xL}, l\Delta_{zL}, p] = \sum_{n=1}^{N_u} h[m\Delta_{xL} - x_n, l\Delta_{zL} - z_n] s^d_n[p] \quad (11)$$

with $s^d_n[p]$ being the time-dependent signal fluctuation in each bubble containing pixel n, and d being the index of the Doppler band. From here on, the processing is performed on each filtered signal, $\hat{b}^d$ and we omit the superscript $[\cdot]^d$ for ease of notation. In Section III, we describe how to exploit statistical properties of CEUS fluctuations over each filtered signal to improve the spatial resolution.

III. Statistical Processing of CEUS Time Series

The statistical blinking of CEUS signals was recently utilized in a method called CEUS SOFI [19], to enhance the spatial resolution of these scans while maintaining high temporal resolution. In CEUS SOFI, the moments of the time series in each pixel were presented together as 2-D images. SUSHI improves upon CEUS SOFI, by exploiting sparsity in the correlation domain on each filtered signal. In this section, we briefly describe the main ideas behind the statistical processing of CEUS scans as presented in [19]. In Section IV, inspired by the SPARCOM method developed for super-resolution florescent microscopy [25], we exploit sparsity in the correlation domain to improve the resolution even further. This enables to achieve super-resolution imaging while dramatically reducing the acquisition time.

We make the following assumptions throughout.

1) For each processed ensemble, the statistics of the measured echoes from the bubbles in each volume cell $s^d_n[p]$ depend only on the time difference τ between the measurements and not on the specific measurement times (i.e., it is a wide sense stationary process).
2) The location of a vessel containing volume cells positioned around $[x_n, z_n], n = 1, \ldots, N_P$ does not change during the short acquisition time of the processed ensemble (and so, no image registration is required).
3) Temporal signal fluctuations in volume cells that belong to different blood vessels are statistically independent.

Following assumptions 1–3, SOFI processing calculates statistical quantities of the CEUS time-series in each pixel and presents them as a single image. For example, the second-order SOFI signal g_2 is produced by estimating the autocorrelation of each pixel in (11) for a prechosen discrete time-lag τ [19]

$$g_2[m\Delta_{xL}, l\Delta_{xL}, \tau] = \sum_n |h[m\Delta_{xL} - x_n, l\Delta_{xL} - z_n]|^2 g_n[\tau] + \sum_{\substack{i,l \\ i \neq l}} h[m\Delta_{xL} - x_i, l\Delta_{xL} - z_i] \cdot \bar{h}[m\Delta_{xL} - x_l, l\Delta_{xL} - z_l] g_{il}[\tau] \quad (12)$$

where $g_n[\tau] = E\{\tilde{s}_n[p+\tau]\overline{\tilde{s}_n[p]}\}$ is the autocorrelation function of the temporal fluctuations of pixel n, and $g_{il}[\tau] = E\{\tilde{s}_i[p+\tau]\overline{\tilde{s}_l[p]}\}$ is the cross correlation of pixels i and j. Here, $\tilde{s}_n[p] = s_n[p] - E\{s_n[p]\}$, n is the pixel index, τ is the discrete predetermined delay of the autocorrelation function, and i and l are indices of (dependent) volume cells located in the same streamline. Bubbles flowing independently in different vessels produce only squared absolute-valued PSF, seen in the first expression in (12) but not cross-terms, seen in the second part of this equation. Being narrower than the original PSF, the squared absolute-valued PSF represents the improved separation between the vessels. The second term shows the wider first order PSFs that smooth the signal from microbubbles flowing along the same vessels. In [19], higher statistical orders were used to further increase the resolution of SOFI images.

The application of SOFI to CEUS scans provides several advantages including a significant SNR improvement [43] and increase in spatial resolution which scales as the square root of the applied statistical order [19]. However, in practice, high-order statistics beyond the fourth moment are rarely used since longer ensembles are needed for estimating high-order statistics; in addition, when using high-order statistics strong echoes mask weaker echoes from adjacent bubbles [18]. The limited improvement in spatial resolution achieved by CEUS SOFI and the ideas presented in SPARCOM [25] motivate the combination of the statistical priors of SOFI with additional

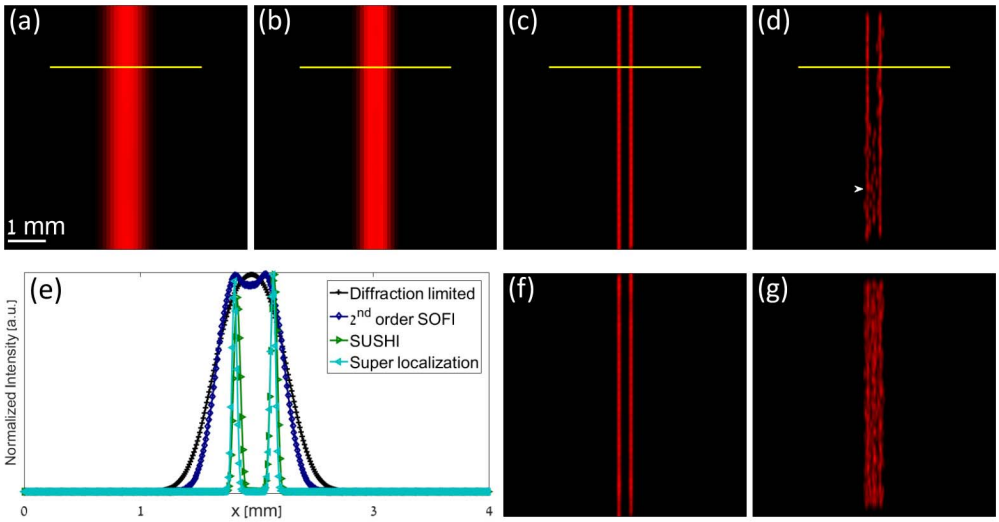

Fig. 1. Simulation showing the resolution capabilities of SUSHI. Flow of low concentration of microbubbles within two nearby narrow tubes is depicted by (a) temporal mean (150 frames), (b) second-order SOFI, (c) SUSHI, and (d) super-localization, compared to (f) higher concentration SUSHI and (g) super-localization reconstructions. (e) Intensity profiles measured along the horizontal yellow lines. The measured ratio between the temporal mean FWHM to the SUSHI/super-localization FWHM is 9.96 and 12.59, respectively, implying an order of magnitude improvement over that of the temporal mean image. Finally, the SUSHI recovery appears smoother compared to the super-localization recovery for both low and high concentrations, without the false-positive detections appearing in super-localization, even at relatively low microbubble concentration (and more so in high concentrations).

priors on the characteristics of the underlying signal of interest, leading to the SUSHI framework for super-resolution CEUS imaging. Using this approach, the vasculature is reconstructed on a grid denser than the grids of CEUS SOFI images, without increasing the required scan time (see Fig. 1).

IV. SUSHI Processing

A. Exploiting Sparsity for Super-Resolution

We now describe the SUSHI processing in detail which exploits sparsity of the underlying vasculature in the correlation domain. Sparse recovery processing is demonstrated by using the correlation-based images calculated from the low-resolution measurements. The key idea in SUSHI is to model the underlying vasculature as composed of point targets on higher resolution grid. We assume that on this grid, the underlying vasculature is sparse. This assumption leads to the formulation of a sparse recovery problem, which is solved with a numerically efficient algorithm. SUSHI can easily be expanded to images of higher order statistics as well (see discussion in Appendix B-A).

Consider the correlation-based CEUS-SOFI image (12). The first term represents the autocorrelation of the temporal fluctuations arising from each microbubble, while the second term constitutes the cross correlation function of temporal fluctuations from adjacent microbubbles flowing within the same vessel in a correlated way. The second term was neglected in the following processing, as it is does not affect the support of the vessels. By posing a sparse recovery problem on the correlation image, we recover a super-resolved map of the vasculature from scans with overlapping CEUS echoes.

To achieve super-resolution, we introduce a new high-resolution grid with spacing $[\Delta_{xH}, \Delta_{zH}]$, such that $[x_n, z_n] = [i_x \Delta_{xH}, i_z \Delta_{zH}]$ for some $i_x, i_z \in \{0, \ldots, N-1\}$, while $[\Delta_{xL}, \Delta_{zL}]$ is referred to as the low-resolution grid. We assume that $\Delta_{xL} = D\Delta_{xH}$ and $\Delta_{zL} = D\Delta_{zH}$ for some $D \geq 1$, and consequently it holds that $N = DM$ (in all of our experiments we fix $D = 8$). Thus, we start from an $M \times M$ CEUS correlation image and reconstruct an $N \times N$ super-resolved image which is D^2 times larger. When studying the structure of the vasculature residing in the imaged plane, the underlying information we wish to obtain is the set of voxels which contain vessels in this high-resolution grid.

Omitting the cross correlation term from (12) (applied to each $\hat{b}^d$), we rewrite it in Cartesian form as

$$g_2[m\Delta_L, l\Delta_L, \tau] = \sum_{i_x, i_z} |h[m\Delta_L - i_x\Delta_H, l\Delta_L - i_z\Delta_H]|^2 g_{i_x,i_z}[\tau]. \quad (13)$$

Substituting $\Delta_{xL} = D\Delta_{xH}$, $\Delta_{zL} = D\Delta_{zH}$ into (13), we have

$$g_2[mD, lD, \tau] = \sum_{i_x, i_z=0}^{N-1} |h[mD - i_x, lD - i_z]|^2 g_{i_x,i_z}[\tau] \quad (14)$$

where Δ_{xL}, Δ_{zL}, Δ_{xH}, and Δ_{zH} are omitted for convenience.

Since we discretized the possible positions of vessels within $N \times N$ pixels, $g_{i_x,i_z}[\tau]$ represents the autocorrelation of pixel $[i_x, i_z]$ on the high-resolution grid, for a prechosen time-lag τ. The possible locations of the vessels are discretized according to the high-resolution grid $i_x, i_z \in [0, \ldots, N-1]$, such that if no bubble is present in some pixel, then its autocorrelation will be zero. By estimating the locations in which $g_{i_x,i_z}[\tau] \neq 0$, a high-resolution estimation of the vascular structure can be achieved. For example, choosing $\tau = 0$, the variance of the fluctuations is estimated using the high resolution grid. Each pixel in the recovered image corresponds to the variance of the echoes originating from this point (or zero, if no echoes are detected).

The above model and the sparsity prior on the underlying vasculature enable us to estimate the locations of the vessels by solving an inverse problem as described below. Following a similar line of computation to that presented in [25], we consider (14) in the discrete Fourier domain, leading to an efficient numerical estimation of the high-resolution image. Note that $g_2[mD, lD, \tau]$ is an $M \times M$ matrix. We denote its 2-D DFT by $G_2[k_m, k_l, \tau]$, where k_m, k_l are $M \times M$ spatial frequencies. Performing an $M \times M$ 2-D DFT on (14) yields

$$G_2[k_m, k_l, \tau] = H[k_m, k_l] \sum_{i_x, i_z=0}^{N-1} g_{i_x, i_z}[\tau] e^{-j\frac{2\pi}{N}k_m i_x} e^{-j\frac{2\pi}{N}k_l i_z} \tag{15}$$

where $H[k_m, k_l]$ is the $M \times M$ 2-D DFT of the $M \times M$ squared, absolute value PSF $|h(xD, yD)|^2$.

Next, we rewrite (15) in matrix-vector notation. To simplify the equation, we perform column-wise stacking (vectorization) of $G_2[k_m, k_l, \tau]$, and denote the result as an M^2 long vector $\boldsymbol{y}[\tau]$, that is $\boldsymbol{y}[\tau] = \text{vec}\{G_2[k_m, k_l, \tau]\}$. In a similar manner, we vectorize the $N \times N$ image statistics on the high-resolution grid $g_{i_x, i_x}[\tau]$ and denote the result as an N^2 long vector $\boldsymbol{x}[\tau]$, so that $\boldsymbol{x}[\tau] = \text{vec}\{g_{i_x, i_y}[\tau]\}, i_x, i_x = 0, \ldots N-1$. Thus, $\boldsymbol{x}[\tau]$ represents the underlying vasculature we wish to recover on the high-resolution grid, and is assumed to be sparse. Rewriting (15) in matrix-vector form yields

$$\boldsymbol{y}[\tau] = \boldsymbol{H}(\boldsymbol{F}_M \otimes \boldsymbol{F}_M)\boldsymbol{x}[\tau] = \boldsymbol{A}\boldsymbol{x}[\tau], \quad \boldsymbol{A} \in \mathbb{C}^{M^2 X N^2}. \tag{16}$$

Here, $\boldsymbol{A} = \boldsymbol{H}(\boldsymbol{F}_M \otimes \boldsymbol{F}_M)$, $\boldsymbol{H}$ is an $M^2 \times M^2$ diagonal matrix with diagonal elements $\{H[0, 0], \ldots, H[\text{M} - 1, \text{M} - 1]\}$, $\otimes$ stands for the Kronecker product and $\boldsymbol{F}_M$ denotes a partial $M \times N$ DFT matrix, created by taking the rows corresponding to the lowest M frequency components of a full $N \times N$ DFT matrix. Additional illustrations and information regarding the Doppler processing and the construction of $\boldsymbol{F}_M$ (Fig. 6) and $\boldsymbol{A}$ are presented in Appendixes A and B.

We solve for $\boldsymbol{x}[\boldsymbol{\tau}]$ in (16) by considering the following optimization problem which includes the prior that $\boldsymbol{x}$ is sparse:

$$\min_{\boldsymbol{x}} \lambda ||\boldsymbol{x}||_1 + \frac{1}{2}||\boldsymbol{y} - \boldsymbol{A}\boldsymbol{x}||_2^2. \tag{17}$$

Here τ is omitted for the sake of simplicity and $\lambda \geq 0$ is a regularization parameter. Exploiting sparsity enables reconstruction of the underlying vascular structure at subdiffraction resolution even without separation of single bubbles. If $\tau = 0$, then $\boldsymbol{x}$ represents the variance of the CEUS signal fluctuations, which is a nonnegative quantity, and consequently the constraint $\boldsymbol{x} \geq 0$ is added.

Many existing algorithms aim at solving (17). We focus on the FISTA [21] algorithm which is known to achieve the fastest possible (worst case) convergence rate for a first-order method, as described by Nesterov [21]. Since we formulated our problem in the (discrete) frequency domain, we are able to evaluate the application of $\boldsymbol{A}$ on a vector using fast Fourier transform (FFT) operations. A detailed description of the SUSHI algorithm is given in Algorithm 1. The sign function in line 2 of the algorithm operates elementwise and is equal 1 for a positive input, zero for a zero input and -1 for a negative input. The calculation of the gradient in Algorithm 1, which involves the application of $\boldsymbol{A}^T$ and $\boldsymbol{A}^T\boldsymbol{A}$ on vectors, can be computed very efficiently, due to our formulation of (16) in the discrete frequency domain (the explicit expression of the gradient is given in step 1 of Algorithm 1). In particular, as shown in detail in [26] in the context of SPARCOM, matrix $\boldsymbol{A}$ does not need to be stored in memory; rather it can be applied directly using FFT operations. Similarly, in the Fourier domain, $\boldsymbol{A}^T\boldsymbol{A}$ admits a structure known as block circulant with circulant blocks, so that it can be applied on vectors directly again using only FFTs leading to a very efficient numerical implementation.

Algorithm 1 SUSHI via FISTA for Minimizing (17)

Input: CEUS movie $\hat{b}$ with P frames, regularization $\lambda > 0$, maximum iterations number K_{MAX}, time-lag τ

Output: $x_{K_{MAX}}$

Statistical pre-processing:

For each pixel in $\hat{b}$ estimate its correlation:

$$g_2[m, l, \tau] = \frac{1}{P - \tau} \sum_{t=1}^{P-\tau} \hat{b}[m, l, t]\, \overline{\hat{b}[m, l, t + \tau]} - \frac{1}{P^2}\left(\sum_{t=1}^{P} \hat{b}[m, l, t]\right)^2$$

Vectorize g_2: $\boldsymbol{y} = vec\{g_2\}$

Initialize: $\mathbf{z}_1 = \mathbf{x}_0 = \mathbf{0}$, $t_1 = 1$, $k = 1$ and $L_f = ||\boldsymbol{A}^T\boldsymbol{A}||_2$

While $k \leq K_{MAX}$ or stopping criteria not fulfilled

1. Calculate $\boldsymbol{q}_k = \boldsymbol{A}^T\boldsymbol{A}\boldsymbol{z}_k - \boldsymbol{A}^T\boldsymbol{y}$ as described in [26]
2. $\mathbf{x}_k = \max\left(\left|\mathbf{z}_k - \frac{1}{L_f}\boldsymbol{q}_k\right| - \frac{\lambda}{L_f}, 0\right) \cdot \text{sign}(\mathbf{z}_k - \frac{1}{L_f}\boldsymbol{q}_k)$
3. $t_{k+1} = 0.5(1 + \sqrt{1 + 4t_k^2})$
4. $z_{k+1} = \mathbf{x}_k + \frac{t_k - 1}{t_{k+1}}(\mathbf{x}_k - \mathbf{x}_{k-1})$
5. $k \leftarrow k + 1$

End

Sparse recovery and in particular super-resolution recovery can also be performed by assuming that $\boldsymbol{x}$ is sparse under different transformations. For example, sparse representation of vascular structures in Haar and Daubechies wavelets has been used in MRI CS algorithms [30]. Another option is to consider super-resolution recovery under total-variation [44] (TV) constraints

$$\min_{\boldsymbol{x}} \lambda \text{TV}(\boldsymbol{x})_1 + \frac{1}{2}||\boldsymbol{y} - \boldsymbol{A}\boldsymbol{x}||_2^2. \tag{18}$$

In its general form, we utilize an analysis-based formulation

$$\min_{\boldsymbol{x}} \lambda ||\boldsymbol{T}^*\boldsymbol{x}||_1 + \frac{1}{2}||\boldsymbol{y} - \boldsymbol{A}\boldsymbol{x}||_2^2 \tag{19}$$

where $\boldsymbol{T}$ stands for the desired transformation such as the discrete wavelet transform or DCT and $(\cdot)^*$ stands for the adjoint operation. Specifically, (19) implies that $\boldsymbol{x}$ has a sparse representation under the transformation $\boldsymbol{T}$, that is $\boldsymbol{x} = \boldsymbol{T}\boldsymbol{\alpha}$, and $\boldsymbol{\alpha}$ is sparse. In the case of a TV prior, we used the TV-FISTA [45] formulation to solve the minimization problem, while for the analysis problem we used the S-FISTA [22] algorithm. The SUSHI images in this paper are generated by solving (17). Comparison to (18) and (19) can be found

in Appendix C. Solutions of (17) and (19) showed similar reconstruction results, which were better in our examples than piecewise-constant images obtained by minimizing (18).

B. PSF Estimation

In practice, to apply the matrix $\boldsymbol{A}$ in (17), the PSF $|h|$ must be estimated first. Generally, even when using high concentrations of US contrast agents, echoes from resolvable bubbles can be expected, at least in small blood vessels with low density flow. In this work, these resolvable echoes were exploited for PSF estimation, using a three-step process. First, the correlation between each image patch and an $M \times M$ template patch is calculated. The template patch can be either manually picked or computed according to the geometry of the transducer and the imaging depth. Patches whose correlation with the template patch is above a predefined threshold are considered relevant. These L patches are automatically aligned to the template using rigid body registration and stacked together to produce an $M \times M \times L$ matrix. Finally, the $M \times M$ PSF is estimated by taking the mean of each pixel, over the L patches. As initialization, patches containing resolvable microbubbles were selected from the *in vivo* scans. The mean of these patches was used as a template for further automatic patch selection.

V. Materials and Methods

We validate SUSHI using numerical phantoms and *in vivo* scans. In these tests, SUSHI achieves spatial resolution gain comparable to that of super-localization approaches, but with short acquisition intervals of only 40–60 ms, compared to tens or hundreds of seconds in super-localization [6], [8]. Using SUSHI, we demonstrate for the first-time subsecond hemodynamic changes in a vascular scan of a rabbit kidney with subdiffraction spatial resolution. Selected frames from a time-lapse movie with a frame-rate of 25 Hz, similar to the frame-rate of clinical hemodynamic Doppler scans [4], are presented in Section VI.

A. Simulations

We first test SUSHI using a numerical phantom simulation, to investigate its possible resolution gain and stability under different concentrations of microbubbles. To compare the results of the proposed method to a known underlying geometry, a 2-D 150–frame-long numerical simulation of signals originating from two closes by parallel vessels is performed. Three Gaussian bubbles were positioned in the right vessel and six in the left vessel. Additional simulations with up to 4 times the number of bubbles tested the effects of higher concentrations (see also additional concentrations in Fig. 10). Here, Doppler processing was not applied, in order to test the separation of vessels with similar flow velocities using sparsity alone. The dimensions of the simulated Gaussian PSF were set according to the experimental PSF estimated from a rabbit kidney scan, as presented in Appendix B. The standard deviations of these microbubbles is defined as $\sigma_x = 0.27$ mm and $\sigma_z = 0.23$ mm in the lateral and axial directions, respectively. The centers of the simulated vessels are separated by $1.2\sigma_x$ to make sure that they are nonresolvable in the temporal mean image. The velocity in the left vessel is defined as $0.25\sigma_z$/frame while the velocity in the right vessel is $0.5\sigma_z$/frame. In this scenario, due to the velocity differences, in some frames microbubble overlap is present, such that two microbubbles are horizontally aligned, and their centroids distance is $1.2\sigma_x$. Initial distance between the bubbles was chosen randomly with a uniform distribution, while preventing the event of connected bubbles. The autocorrelation of the simulated complex signals is calculated together with the temporal mean of the envelope signal in each pixel.

SUSHI images are also compared to super-localization images generated throughout this paper using the Image-J software [46] and the ThunderSTORM plug-in [47]. In essence, this plug-in finds local maxima points and performs a nonlinear fit to a Gaussian for each such detection, to achieve sub-pixel precision. In an iterative manner, the Gaussian width is also estimated in the process. Specifically, in this study, we performed this fit via the weighted least squares option. Prior to the fitting procedure, this code denoised the input data using a wavelet based built-in denoising procedure with B-spline of order 2 and scale 3. Both SUSHI and the super-localization recovery were smoothed, as is customary in single molecule microscopy, with the same Gaussian kernel. A bifurcation simulation similar to the first bifurcation in [48] was also performed (see Fig. 11).

B. In Vivo Ultrafast Imaging

The *in vivo* scans presented throughout this paper belong to a New Zealand white rabbit model: plane wave inversion Doppler (PID) [39] was used to image normal vessels in the kidney of healthy rabbits. All the scans were acquired using a clinical Aixplorer US system (Supersonic Imagine, Aix-en-Provence, France) and an L15-4 linear probe transmitting at a PRF of 5 kHz. Only the central part of the elements is used upon reception due to channel limitation. The carrier frequency of the transmitted single cycle pulses was 4.5 MHz and a mechanical index of 0.06 was used to reduce the burst rate of the microbubbles. Definity (Lantheus Medical Imaging Inc., N. Billerica, MA, USA), a clinically approved contrast agent, was used at a clinical concentration of 10 μL/Kg. Following the injection of 0.5 mL of this contrast agent into the ear vain of the rabbit, an additional 1 mL of saline was used to flush it. All the protocols were approved by the Sunnybrook Research Institutional Review Board.

The initial step in the processing of the received IQ data was the weighted summation of the echoes from different pulses that compose the PID sequence. This process cancels out the linear part of the signal and maintains the nonlinear bubble related signal. The single channel data is then beamformed to produce a 2-D + time cine matrix. Fast time (axial direction) 2–12-MHz finite-impulse response bandpass filter was applied to remove noise outside the passband of the transducer. Next, Doppler (slow time) processing was performed to remove the static clutter from the moving blood and to provide separation between small vessels with blood

flowing in opposite directions. A sixth-order Butterworth filter with a stopband of 0.03PRF was used as the clutter filter (wall filter). This threshold is selected since it provides good separation between flow and clutter.

VI. Results

A. Simulations

The numerical simulation covered a wide range of contrast agents' concentrations. In practice, even when high concentrations of contrast agents are injected and many microbubbles are found in the imaging plane, separated microbubbles can be frequently found in specific locations containing small vessels. The simulation depicted in Fig. 1(a)–(d) represents a CEUS patch with such low concentration of microbubbles within two adjacent vessels. Fig. 1(a) shows the temporal mean image, created by averaging the envelope of all 150 frames included in the movie. Fig. 1(b) illustrates the second-order SOFI reconstruction (zero time-lag), and Fig. 1(c) and (d) shows the SUSHI and super-localization reconstructions, respectively. In contrast to Fig. 1(a)–(d), Fig. 1(f) and (g) depicts the SUSHI and super-localization reconstructions for high local concentration, respectively. Judging the panels, SOFI resulted only in a slight decrease in the intensity between the two streamlines, while SUSHI and the super-localization technique fully resolved them. Fig. 1(e) provides further support to this conclusion, by presenting an intensity cross section along the lateral direction for the low concentration scenario [yellow line in Fig. 1(a)–(d)]. The plus head (black line) in Fig. 1(e) corresponds to the temporal mean image, diamond-head (blue line) to the second-order SOFI image and the right head (green line) and left head (turquoise line) to the SUSHI and super-localization images, respectively. Both SUSHI and super-localization techniques resolve the two lines, while the second-order SOFI does not. (A very minor dip is present.) Furthermore, the SUSHI and super-localization profiles depict an almost perfect match.

To quantify the resolution enhancement, the full-width at half-maximum (FWHM) ratio between that of the temporal mean and SUSHI/super-localization profiles (right peak) is measured as 9.96 and 12.59, respectively. The SUSHI FWHM ratio implies a resolution increase by an order of magnitude beyond the classical resolution of the scanner, similar to the results presented previously using super-localization [8].

Nevertheless, it is important to note that even at this simulation of low contrast agent concentration, super-localization processing produces false positive detection, marked by the white arrow at the lower part of Fig. 1(d), which are absent in the SUSHI image. Similar results were also observed in the bifurcation simulation (Fig. 11). This effect worsens as the concentration increases [Fig. 1(g) and (f)]. The rate of false positive detections increases with the bubbles concentration for super-localization [Fig. 1(g)], while the SUSHI recovery [Fig. 1(f)] seems similar to the recovery for low concentrations. We conclude that SUSHI operates better in higher concentrations than super-localization. Thus, SUSHI is able to process scans of higher concentrations of contrast agents, which leads to a dramatic reduction in the acquisition time, while producing super-resolved images of the vasculature.

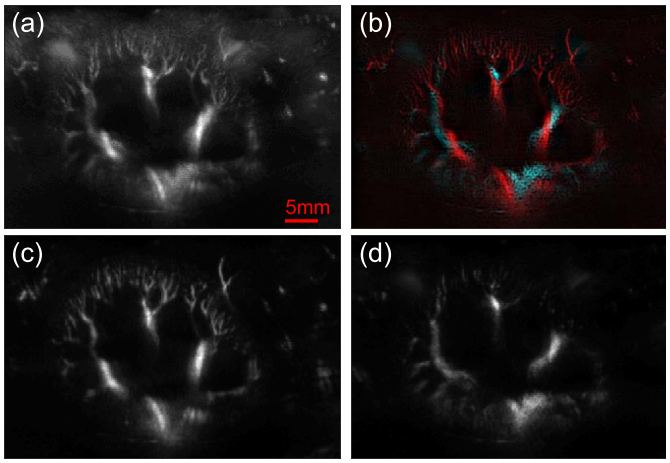

Fig. 2. Decomposition of the vasculature using Doppler preprocessing. (a) Temporal mean image of the kidney. (b) SUSHI reconstruction. Red indicates negative flow and cyan positive flow with respect to the transducer. (c) Correlations SOFI image of the negative flow. (d) Correlations SOFI image of the positive flow. (c) and (d) display nearby vessels with opposite flow velocities are decomposed using Doppler processing. Comparing (c) and (d), Doppler processing can clearly distinguish between overlapping blood vessels according to their flow directions. Moreover, (b) shows clear SUSHI high-resolution reconstruction of the entire kidney with separation to positive and negative flows.

B. In Vivo Experiments

To validate the performance of SUSHI when applied to *in vivo* scans, two scans previously presented [19], [49] are reprocessed. These scans include noise, out-of-plane reflectance and depict the true nonlinear behavior of the injected microbubbles at high US contrast agent concentrations usually used in the clinic.

The capability of Doppler processing to separate between adjacent vessels with different flow velocities is demonstrated in Fig. 2. Here, SUSHI is implemented on a rabbit kidney scan containing 150 frames. The temporal mean image of the kidney is presented for reference in Fig. 2(a). The second-order correlation images of the positive and negative flow components are displayed in Fig. 2(c) and (d), respectively. These two images show different vascular structures with higher resolution compared to the temporal mean image. Fig. 2(b) presents the SUSHI reconstruction of the entire kidney, divided into both flow directions. Fig. 2(b) serves to emphasize the power of SUSHI to process entire organs, without any restrictive assumptions on the geometry of the blood vessels. By examining Fig. 2(a)–(d), it can be seen that, indeed, the intertwined vasculature of arteries and veins is separated. Therefore, Doppler-based filtering serves as an important preprocessing step. CS processing is then performed on each image separately, to achieve better depiction of the blood vessels, and their flow directions. Although some of the largest blood vessels appear slightly grainy, we emphasize that these blood vessels are considerably larger than the diffraction limit, and are not the focus of the resolution enhancement performed by SUSHI. Improving their visual quality is a matter for future work. To gain a detailed comparison between the spatial resolution enhancement of different approaches, we turn to perform our analysis on specific regions of interest.

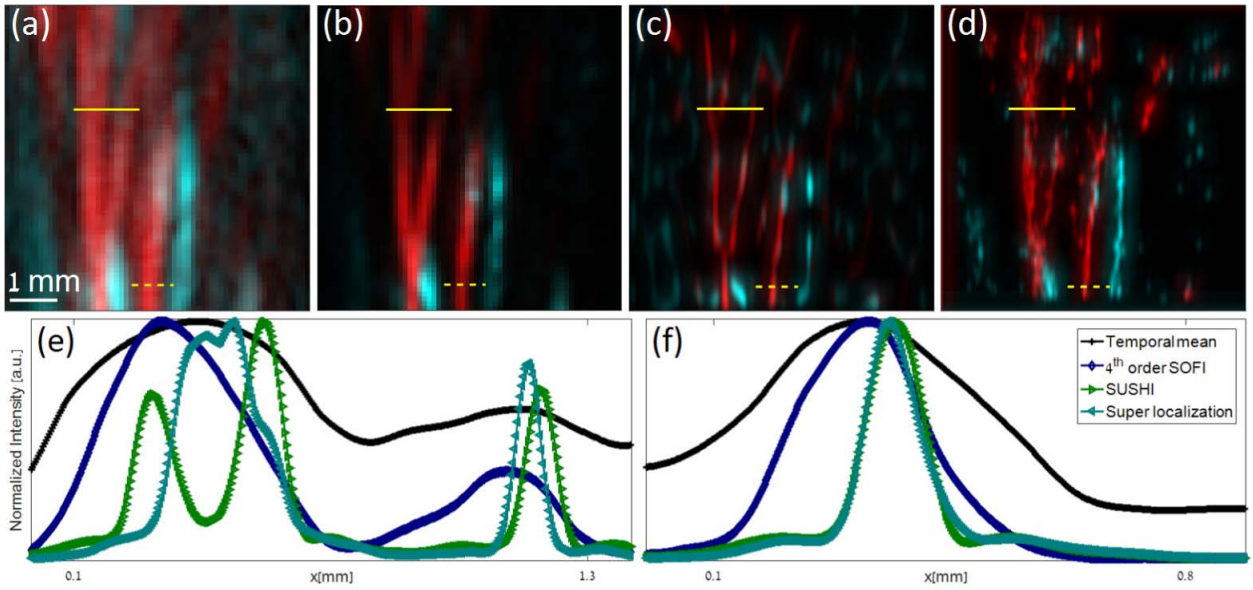

Fig. 3. Spatial resolution comparison. Blood vessel bifurcations, appearing in a scan acquired with high concentration of contrast agents, are depicted as (a) temporal mean, using 150 frames, (b) fourth-order SOFI, (c) SUSHI, and (d) super-localization. Red and cyan depict hemodynamic flow from and toward the transducer, respectively. Comparing visually, the super-localization image seems very noisy and unclear, while temporal mean and SOFI images have degraded resolution compared with SUSHI. SUSHI exhibits the clearest image of the vasculature, presenting a sharp, almost noiseless reconstruction, compared with the other methods. (e) and (f) Intensity profiles measured along the solid and dashed yellow lines on (a)–(d). All profiles were taken with respect to the red blood vessels only. (e) shows that in high density areas (e.g., bifurcations), SUSHI is superior, while in low density areas [e.g., isolated vessel in (f)], SUSHI exhibits comparable spatial resolution to super-localization.

Fig. 3 presents a comparative processing of a patch taken from the kidney scan presented in Fig. 2. In this scan, UCA overlap is present in most frames. Fig. 3(a)–(d) shows temporal mean, fourth-order SOFI (zero time-lag, absolute value), SUSHI and super-localization reconstructions, respectively. Red and cyan blood vessels correspond to negative and positive flow with respect to the transducer. Judging visually, the SOFI image seems clearer than the temporal mean image, though the resolution enhancement is limited. The SUSHI reconstruction is very well-defined and sharp, depicting clear bifurcations and intertwined blood vessels. In contrast, the super-localization image seems noisier without a clear depiction of the bifurcation. This happens since in this scan UCA overlap is present, which emphasizes its limitation in the case where high densities are used to reduce acquisition time bellow 100 ms.

Fig. 3(e) and (f) presents selected intensity profiles of the four methods along the solid and dashed yellow lines, respectively. (Profiles were taken with respect to the red blood vessels.) Fig.3(e) and (f) supports the conclusions drawn from the visual comparison. Fig. 3(e) shows that SUSHI (right arrow, green) clearly separates the two leftmost blood vessels. The temporal mean and SOFI profiles (plus head, black and diamond blue, respectively) do not exhibit such separation. The super-localization profile does not produce a clear depiction of the bifurcation. On the other hand, Fig. 3(f) demonstrates that when isolated blood vessels are considered and clear UCA separation is evident, the resolution of SUSHI, even on experimental scans, is similar to that of the super-localization recovery, though slightly lower.

The measured ratios between the temporal mean FWHM and the SUSHI/super-localization FWHM is 4.55 and 4.97, respectively, almost 5 times better than that of the original temporal mean. Here, the change in FWHM does not reflect the full increase in resolution since it is affected by the width of the blood vessels.

After comparing the spatial resolution of SUSHI and super-localization images, we proceed to demonstrate the ability of SUSHI to produce subdiffraction movies with a high temporal resolution of 25 Hz, capturing changes in the imaged flow pattern. Fig. 4(a)–(d) presents four fourth-order SOFI images (zero time-lag) from a longer rabbit scan, injected with the contrast agent concentration similar to that used in the clinic. Each Fig. 4(a)–(d) is composed from 100 consecutive frames from the 1000 frames included in the complete scan. Corresponding SUSHI reconstructions are presented in Fig. 4(e)–(h). The four high-resolution SUSHI images illustrate a temporal resolution of 25 Hz. The white arrows in Fig. 4(f) and (g) point to a clear bifurcation which is considerably less visible, and with poorer resolution in the corresponding SOFI images. This bifurcation vanishes in Fig. 4(h), suggesting a difference in the vasculature captured during later parts of this subsecond scan. This observation shows the ability of SUSHI to monitor hemodynamic changes in a high spatiotemporal resolution.

Fig. 4(i) illustrates the spatial shift ($\sim$0.5 mm) in the position of the blood vessel [Fig. 4(e) in green and Fig. 4(h) in purple], indicated by the white arrow, over a span of 240 ms (40 ms frame rate). Since super-localization-based techniques operate with longer acquisition periods, they require motion compensation to be applied to the localizations to reduce

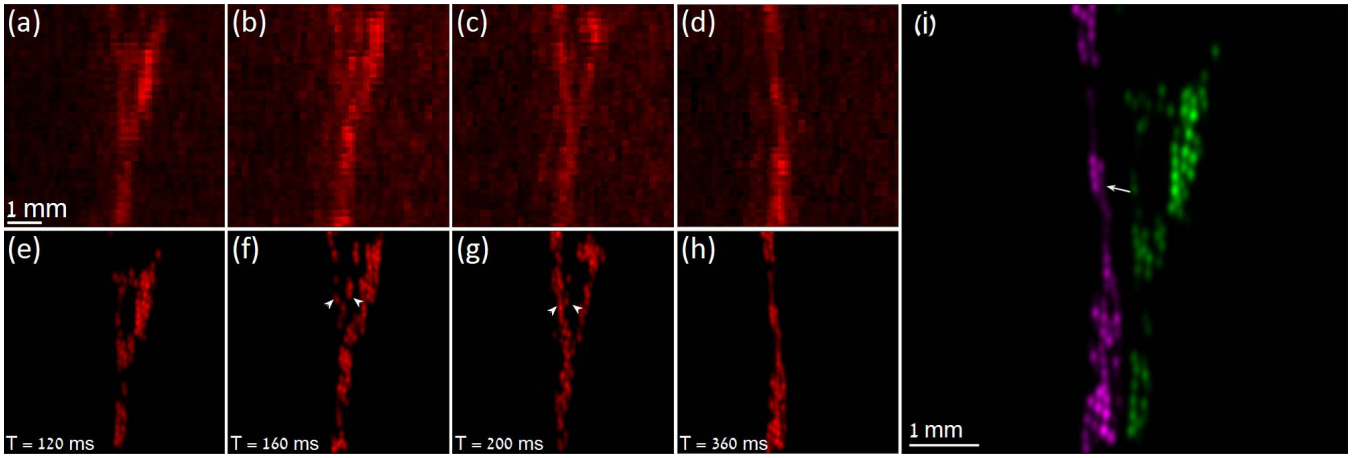

Fig. 4. Demonstration of the high temporal resolution of SUSHI. (a)–(d) Four fourth-order SOFI snapshots (zero time lag) of the same bifurcation of a blood vessel in a kidney of a white New Zealand rabbit, injected with US microbubbles, at different times. Here, very short ensembles of 100 frames were used for each image. (e)–(h) Times of the snapshots are given in the lower left corners, which present the corresponding SUSHI reconstructions to (a)–(d). (i) Super-imposed image of (e) and (h) in green and purple, respectively, spanning a temporal duration of 240 ms (40-ms frame rate). Bifurcation of blood vessels marked by the white arrow heads can be clearly seen in (f) and (g), which is clearly less visible in the corresponding SOFI (b) and (c). The white arrow in (i) serves to emphasize the lateral translation of the blood vessel during a period of 400 ms. This example depicts the ability of SUSHI to image *in vivo* fine vasculature with a high spatiotemporal resolution.

the overall localization error. SUSHI does not require such compensation in order to provide super-resolved time-lapse imaging of fast hemodynamic changes, but might benefit from it if the acquisition is extended when aiming to maximize the percentage of the vasculature imaged during the scan of low perfused tissues, such as tumors.

VII. Discussion

In this work, SUSHI is shown to produce images with exceptional combination of spatial super-resolution and high temporal resolution. This is achieved by relying on the ability to separate close-by vessels according to their Doppler velocities; the independence of CEUS fluctuations originating from different vessels; and by exploiting sparsity in the correlation domain. This prior information enables the proposed framework to produce an unprecedented spatiotemporal resolution tradeoff: a tenfold increase in spatial resolution and high temporal resolution. In cases where high UCA concentrations are considered, SUSHI produces a clear depiction of the vasculature with subsecond acquisition times, compared to typically a few minutes in super-localization scans [6], [8]. When well isolated blood vessels were analyzed, FWHM values of SUSHI were comparable to those of super-localization although slightly lower.

Fast super-resolution opens a vast range of opportunities for future applications and follow-up studies. Foremost, it facilitates functional (hemodynamic) super-resolution imaging that could bridge, for example, between cerebral anatomical super-resolution and functional neural imaging. In addition, it solves several important practical limitations that currently hinder wide clinical use of current CEUS super-resolution techniques. First, SUSHI acquisitions can be performed between breaths without the need for long breath-holds, which are unmanageable for many patients. Second, the numerically efficient implementation described in Appendix B, and the potential for parallel processing of many image patches could facilitate an in-clinic fast reconstruction process. Finally, when using scanners with limited computational resources, a reduction of almost 2 orders in the number of acquired frames compared to super-localization techniques means lower amounts of data to store and process.

SUSHI shares an inherent physical limitation of all CEUS imaging methods with short acquisition times, even when high US contrast agent concentrations are used: certain vessels with very low flow velocities might not contain microbubbles during the imaging interval. This is also true for both SUSHI and CEUS imaging methods with lower CEUS concentrations and longer acquisition times, no matter what processing method is applied. Although the use of high concentrations of US contrast agents in this work maximizes the portion of the vessels included in the scan within a given acquisition time, it cannot ensure a full coverage of the vasculature if very short acquisition intervals are needed. Incorporating microbubbles tracking over several frames within the super-localization framework can improve microbubble detection and ULM estimations which could be important specifically in short CEUS acquisitions [48]. The integration of sparsity and UCA motion kinematics is a topic of continuing research [50].

Finally, in this study, SUSHI was implemented using fast plane-wave imaging to detect fast hemodynamic changes. Currently, the use of fast plane-wave imaging is not widespread, mainly due to hardware limitations. When considering variance estimation, as was presented here, SUSHI can in principle also be applied with lower rate commercially available scanners, using wide beam imaging for example. In the general sense, sparsity can even be used in the processing of images when RF signals are not accessible [50].

VIII. Conclusion

This work presents a new and improved tradeoff between spatial and temporal resolutions in CEUS imaging: short acquisitions of only tens of milliseconds, with a 25 Hz temporal resolution, and improved super-resolution abilities with 64-fold increase in pixel density and up to a tenfold increase in

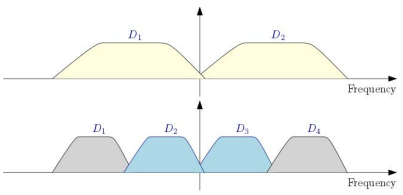

Fig. 5. Separation to Doppler frequency bands using temporal bandpass filters. Two Doppler filters (top). Four Doppler filters (bottom).

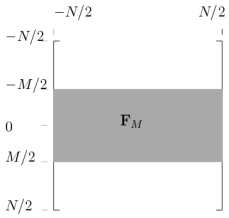

Fig. 6. Partial discrete Fourier matrix of low-frequency components.

spatial resolution. Drawing inspiration from SPARCOM, these results are achieved by a CS framework that combines prior knowledge on the temporal fluctuations of the received signal, alongside the sparse nature of the underlying signal. The proposed approach is characterized by short acquisition times, computationally efficient implementation, and reduced memory burden, which together could simplify the clinical adaptation of super-resolution CEUS. In addition, the enhanced spatiotemporal resolution provides researchers with a new set of tools that may enable, for example, the investigation of malignant hemodynamic patterns, super-resolution imaging of cardiac vasculature, and the monitoring of fast hemodynamic changes in functional neural scans.

Appendix A
Supporting Figures for the Theoretical Derivations

Fig. 5 illustrates spectral decomposition of the continuous Doppler spectrum into several bands for several possible selections of the temporal bandpass filters, described in (10). The upper illustration depicts two symmetric filters D_1 and D_2, separating the spectrum into positive flow and negative flow, with respect to the transducer. The lower figure shows four filters $D_1 - D_4$ separating the spectrum into four categories. This decomposition provides both flow direction and in each direction two flow categories. For example, D_3 indicates slow, positive flow with respect to the transducer, while D_4 indicates fast, positive flow. The same holds for D_2 and D_1 for negative flow. Each such filter is applied on every pixel's time trace, separately. Additional decompositions can also be performed, such that each filtered signal occupies a narrower velocity range.

Fig. 6 depicts the partial discrete Fourier matrix, as described in Section IV-A. The matrix $\boldsymbol{F}_M$ is constructed by first generating a full $N \times N$ DFT matrix and then removing some of its rows. In this illustration, the zero frequency is at the middle of the matrix, negative frequencies correspond to the upper half of rows, and positive frequencies correspond to the lower half of rows. The matrix $\boldsymbol{F}_M$ consists only of the M rows from $-M/2$ to $M/2$, as marked by the gray rectangle.

Appendix B
Supporting Material for Implementation of SUSHI

A. Use of Higher Statistical Order in SUSHI Processing

Sparse recovery can be used not only for the correlations image, but theoretically for any statistical image, e.g., fourth-order images, in which the value of each pixel is the fourth moment of its time trace. Thus, (14) in the main text will consist of a super-position of the absolute PSF $|h|$ raised to the power of 4 instead of 2, and g_{i_x,i_z} will consist of the fourth-order moment estimation of the emitters' fluctuations. SUSHI will then be applied using an estimate of the PSF raised to the power of 4 when minimizing (17)–(19).

In practice, we refrain from high-order statistical estimation and demonstrate SUSHI using correlations only, since statistical estimation of high-order moments requires an exponentially increasing number of frames to retain the same SNR level. This in turn reduces the temporal resolution of SUSHI, since longer movie ensembles are required for the estimation process. Thus, for the sake of simplicity and to achieve good temporal resolution, we restricted the demonstration in this paper to second-order statistics, which can be estimated from a relatively low number of frames, as we demonstrate in Section VI. There we show a significant improvement in the spatial resolution compared to the diffraction limit, with a subsecond temporal resolution.

B. Forward Problem in the Matrix-Vector Form

For convenience of the reader, we present here the forward problem (16) in the matrix-vector form in a more explicit way. Specifying separately each element of the PSF matrix $\boldsymbol{H}$ and the vectors $\boldsymbol{y}$ and $\boldsymbol{x}$, we get

$$\begin{bmatrix} y_1(\tau) \\ \vdots \\ y_{M^2}(\tau) \end{bmatrix} = \begin{bmatrix} H[0,0] & 0 & 0 \\ 0 & \ddots & 0 \\ 0 & 0 & H[M-1,M-1] \end{bmatrix} \times (\boldsymbol{F}_M \otimes \boldsymbol{F}_M) \begin{bmatrix} x_1(\tau) \\ x_2(\tau) \\ \vdots \\ x_{N^2}(\tau) \end{bmatrix} \quad (20)$$

where $\boldsymbol{y}$ is the temporal autocorrelation vector, calculated from the data measured on the low-resolution grid, and $\boldsymbol{x}$ is the sparse representation vector that we want to estimate (on the high-resolution grid). M is the width and length of the low-resolution grid, N is the width and length of the high-resolution grid, and τ is the discrete time lag used for the autocorrelation calculation.

C. PSF Estimation

In this section, we provide an example of the estimated PSF, using the procedure described in Section IV-B. An example of the real component of an automatically detected patch

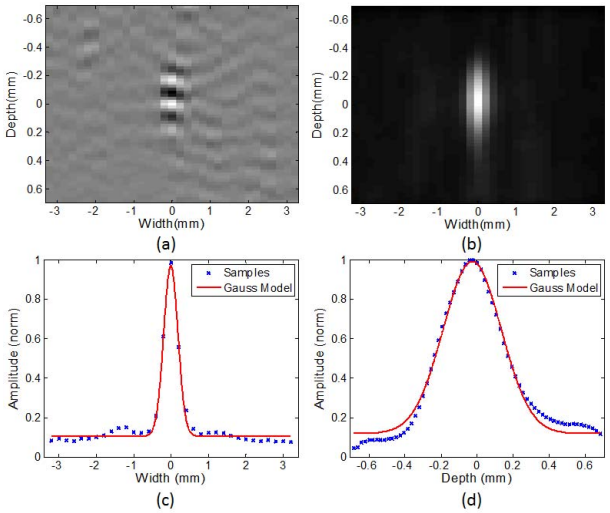

Fig. 7. PSF estimation from resolvable microbubbles. (a) Patch including a single resolvable microbubble. (The real part of the signal is displayed.) (b) Absolute value of the final estimation of the PSF. (c) Lateral section through the estimated PSF showing sidelobes. (d) Axial cross section through the estimated PSF showing the ringing of the transmitted pulse. Clearly, there is some mismatch to the simplified Gaussian model. However, SUSHI can operate adequately with both the estimated PSF (see Fig. 3) and a Gaussian estimate (see Fig. 4).

with a recoverable microbubble is depicted in Fig. 7(a). The modulation of the pulse can be clearly seen. The final estimated PSF is presented in Fig. 7(b) in its absolute value. The amplitude of cross sections through this PSF, in the lateral and axial directions, is presented in Fig. 7(c) and (d), respectively, along with their Gaussian approximation. The limitation of the Gaussian approximation is evident by looking at the additional details appearing in the estimated PSF. These details include sidelobes [Fig. 7(c)] in the lateral direction and asymmetric structure, related to the ringing of the transducer, in the axial direction [Fig. 7(d)]. The estimated PSF is then used in the SUSHI algorithm to recover the underlying vasculature with subdiffraction resolution.

APPENDIX C
SUPPORTING *In Vivo* RESULTS

A. Additional In Vivo Example

In this section, we show an additional example of the high-resolution reconstruction obtained by SUSHI, when high densities are used. Fig. 8 shows an additional patch of sub diffraction sized blood vessels, taken from the same kidney scans (150 frames) presented in Figs. 2 and 3. The vessels in red contain negative flow with respect to the transducer, while vessels in cyan illustrate the positive flow.

Fig. 8(a)–(d) depicts four reconstructions: temporal mean, fourth-order SOFI (zero time-lag, absolute value), SUSHI and super-localization, respectively. Judging visually, the SUSHI recovery seems the sharpest of all recoveries, showing clear bifurcations, which are missing in the temporal mean and SOFI recoveries. Since the microbubbles density is high (clinical dose), the super-localization technique involves many false detections and results in a noisy and unclear image.

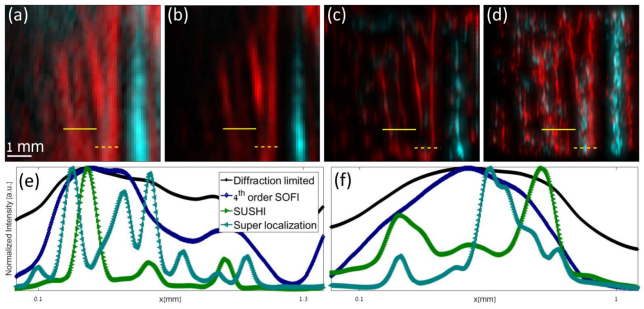

Fig. 8. Additional spatial resolution comparison. Blood vessel bifurcations are depicted with (a) temporal mean, using 150 frames, (b) fourth-order SOFI, (c) SUSHI, and (d) super-localization. Red and cyan depict hemodynamic flow from and toward the transducer. (e) and (f) Two intensity profiles measured along the yellow solid and dashed lines on (a)–(d). All profiles were taken with respect to the red blood vessels only.

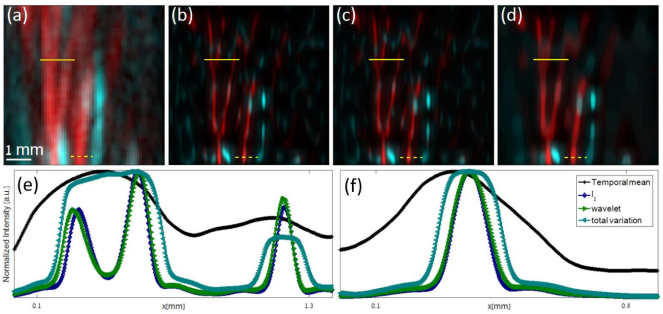

Fig. 9. Sparse recovery under different sparsity assumptions. Blood vessel bifurcations are depicted with (a) temporal mean, using 150 frames, (b) SUSHI recovery using (17), (c) SUSHI recovery using (19), and (d) SUSHI recovery using (18). Red and cyan depict hemodynamic flow from and toward the transducer. (e) and (f) Intensity profiles are given, corresponding to the yellow solid and dashed lines in (a)–(d), respectively. Comparing visually, (b) and (c) show similar reconstruction (l_1 and wavelet), while (d) (TV) shows a reconstruction with degraded resolution. (e) and (f) support this observation. For example, (e) shows a clear bifurcation for the l_1 and wavelet recoveries, which is absent in the TV image.

Fig. 8(e) and (f) depicts selected intensity profiles along the yellow solid and dashed lines, respectively. The temporal mean profile is given by the plus-head, black line, fourth-order SOFI by the blue diamond-head line, SUSHI by the green right-arrowhead and super-localization by the turquoise, left-arrowhead. Fig. 8(e) and (f) serves to illustrate that SUSHI detects subdiffraction blood vessels, which are not depicted by the temporal mean and SOFI reconstructions, while achieving clearer depiction compared to super-localization, when high concentrations are used. A clear depiction of bifurcations is seen in the SUSHI profiles [e.g., three blood vessels on Fig. 8(e)], while the super-localization profiles seem noisy and contain many false detections of blood vessel.

B. Reconstruction With Different Sparsity Priors

In this section, we provide a comparison between SUSHI recoveries under different sparsity assumptions. We compare with the same data presented in Fig. 3. In all cases, sparse recovery was performed using $\lambda = 0.5$ and 150 iterations.

Fig. 9(a) shows the temporal mean image and Fig. 9(b)–(d) shows SUSHI recoveries. Reconstructions were performed using (17), (19), and (18), respectively (l_1, wavelet and TV). The wavelet filter used in the reconstruction of Fig. 9(c) is a Daubechies wavelet with 16 taps, and we use a single level of decomposition. Clearly, Fig. 9(b) and (c) shows similar images and achieve similar spatial resolution. The reconstruction in Fig. 9(d), using the TV norm, yields a reconstruction with poorer spatial resolution. Fig. 9(e) and (f) shows intensity profiles which further support our analysis. Both recoveries in Fig. 9(b) and (c) (l_1 and wavelet) managed to resolve the left bifurcation in Fig. 9(e), while the reconstruction using the TV norm did not (though it achieved better resolution than the temporal mean image). Even in isolated blood vessels [see Fig. 9(f)], the width of the l_1 and wavelet reconstructions was similar and narrower than the TV reconstruction.

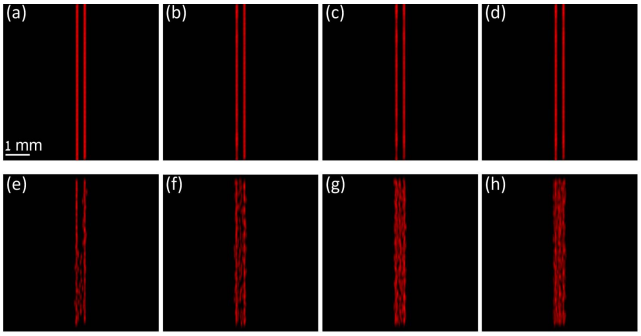

Fig. 10. Simulation results of increased microbubble densities. (a)–(d) SUSHI recoveries of the two streamlines presented in Fig. 1, and recoveries with increasing microbubble density of 2, 3, and 4 times the original concentration, respectively. (e)–(h) Corresponding super-localization recoveries. It can be observed that as the density of flowing microbubbles increases, super-localization techniques fail due to the strong overlap between the echoes of the bubbles. On the other hand, in all cases, SUSHI manages to recover the two streamlines similarly, for every density presented here.

APPENDIX D
ADDITIONAL SIMULATIONS

A. Increased Microbubble Densities in Numerical Simulations

Increasing the concentration of microbubbles injected into the body increases the probability of at least one microbubble flowing inside a given vessel during the duration of the US scan. Therefore, using the highest clinically approved concentration maximizes the portion of the vasculature detected during a certain imaging interval. This is true no matter what processing method is applied to the acquired CEUS data. Therefore, with increased temporal resolution being the focus of our study, the maximal clinically approved US contrast agent concentration is used in all the *in vivo* scans. To test the capabilities of this method over a wide range of concentrations, numerical simulations with a different number of microbubbles were produced.

In this section, we compare the performance of SUSHI against super-localization using data generated by a set of simulations with increased microbubble densities, moving along the same two streamlines presented in Fig. 1. Four movies were generated, 150 frames each, of microbubbles flowing along the two streamlines. In the original simulation, three Gaussian bubbles were positioned in the right vessel and six in the left vessel. Here, each movie has increased microbubbles density. The second movie has twice the density compared to the first, the third movie has three times the density, and the fourth movie has four times the density. Fig. 10(a)–(d) shows the corresponding SUSHI reconstructions, while Fig. 10(e)–(h) illustrate the corresponding super-localization recoveries, for increasing densities, respectively. All reconstructions were smoothed with the same Gaussian kernel, so that the comparison is performed under similar conditions.

Judging the recoveries in Fig. 10(a)–(h), one observes that for all these concentrations SUSHI produces successful reconstructions, while a clear degradation in the super-localization estimations is evident. In Fig. 10(g) and (h), one can note many false positives, and it is nearly impossible to clearly separate the two streamlines, thus demonstrating the limitations of super-localization when applied to CEUS scans with high CEUS concentrations. Figs. 8 and 10 substantiate the conclusions drawn that when using high densities, the performance of SUSHI is superior compared to the other methods. Higher concentrations lead to a reduction in the number of frames required to create a single super-resolved image, which in turn leads to an increase in the temporal resolution.

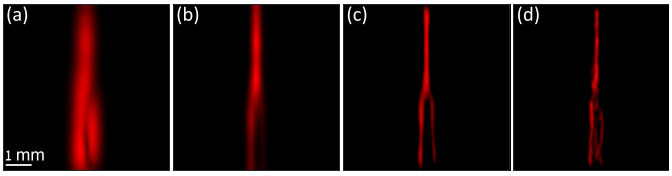

Fig. 11. Simulation results of bifurcating blood vessel. Blood vessel bifurcations are depicted with (a) single frame from the movie, absolute value, (b) fourth-order SOFI recovery, zero time-lag, (c) SUSHI recovery using (17), and (d) super-localization recovery. SUSHI manages to clearly detect the bifurcation better than the SOFI image, while showing its clear depiction, unlike the super-localization image.

B. Bifurcation Simulation

In this section, we provide an additional simulation comparison between SUSHI, SOFI and super-localization, of a bifurcation blood vessel. Similar to the first bifurcation in [48], the width of the main vessel is 40 μm with a peak velocity of 15 mm/s and the width of the secondary vessels was 25 μm. The PSF was identical to the one in Figs. 1 and 10, and a total of 600 frames were simulated. Initial location along the cross section of the vessel was uniformly randomly selected. Temporal density is identical as in the simulation of two parallel blood vessels (Fig. 1) and in the branches of the bifurcating vessels, on average. Fig. 11(a)–(d) shows a single frame from the movie, where significant UCA overlap is evident, fourth-order SOFI image, SUSHI image and super-localization recovery. Similar conclusions can be deduced here also. Clearly, SUSHI outperforms the SOFI and temporal mean images, by clearly detecting the bifurcation (much earlier than

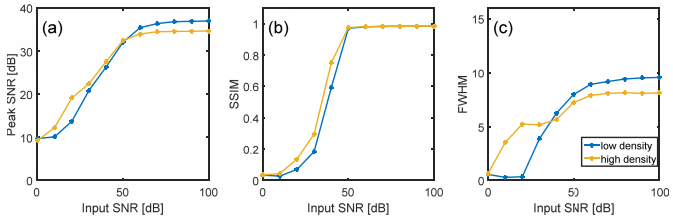

Fig. 12. PSNR, SSIM, and FWHM values for low and high UCA density simulations. (a) PSNR values in dB for SUSHI. (b) SSIM values. (c) FWHM ratios for the SUSHI reconstructions. It can be observed that, as expected, as the SNR increases, the metrics values for SUSHI increase and achieve high PSNR and SSIM values, as well as high values of FWHM ratios, for both concentrations.

the SOFI image). The SUSHI recovery is also better than the super-localization recovery, in which the depiction of the bifurcation in unclear and with artifacts.

Appendix E
Noise Analysis

We next use two of the simulations presented in Fig. 1 (lowest and highest UCA concentration simulations) to test the performance of SUSHI with varying SNR conditions. To perform a fair analysis, we normalize the intensity of each movie frame to 1 and define the SNR as $\text{SNR} = 1/\sigma^2$, where σ is the standard deviation of the noise. We add white Gaussian noise for increasing SNR values to the movie and performed SUSHI recovery. Each recovery is then smoothed with the same kernel as before (postprocessing) and its peak intensity is normalized to one. We compute three metrics, peak SNR (PSNR) and structural similarity index (SSIM) against the noiseless SUSHI recovery, and the FWHM ratio computed as the ratio between the FWHM value of the temporal mean image, divided by the FWHM of the corresponding SUSHI recovery.

Fig. 12 depicts these values as a function of increasing SNR. It can be observed from Fig. 12(a)–(c) that as the SNR increases, the quality of the SUSHI recoveries, as measured by the PSNR, SSIM, and FWHM ratio metrics increases, for both concentrations. For SNR values of 20–30 dB and higher, SUSHI performs well and achieves PSNR values above 20 dB, SSIM values close to one (not really affected by different concentrations) and a FWHM ratio of ∼8–10, indicating a resolution gain of ∼8–10 times better than the temporal mean image, for both concentrations. As the concentration increases, the FWHM ratio decreases [Fig. 12(c)], but still, an order of magnitude improvement in the FWHM ratio is evident for high SNR values.

References

[1] J. M. Hudson *et al.*, "Dynamic contrast enhanced ultrasound for therapy monitoring," *Eur. J. Radiol.*, vol. 84, no. 9, pp. 1650–1657, Sep. 2015.
[2] C. B. Conti, M. Giunta, D. Gridavilla, D. Conte, and M. Fraquelli, "Role of bowel ultrasound in the diagnosis and follow-up of patients with Crohn's disease," *Ultrasound Med. Biol.*, vol. 43, no. 4, pp. 725–734, 2017.
[3] C. N. Hall *et al.*, "Capillary pericytes regulate cerebral blood flow in health and disease," *Nature*, vol. 508, no. 7494, pp. 55–60, 2014.
[4] E. Macé, G. Montaldo, I. Cohen, M. Baulac, M. Fink, and M. Tanter, "Functional ultrasound imaging of the brain," *Nature Methods*, vol. 8, no. 8, pp. 662–664, 2011.
[5] R. K. Jain, "Normalization of tumor vasculature: An emerging concept in antiangiogenic therapy," *Science*, vol. 307, no. 5706, pp. 58–62, 2005.
[6] C. Errico *et al.*, "Ultrafast ultrasound localization microscopy for deep super-resolution vascular imaging," *Nature*, vol. 527, no. 7579, pp. 499–502, 2015.
[7] M. A. O'Reilly and K. Hynynen, "A super-resolution ultrasound method for brain vascular mapping," *Med. Phys.*, vol. 40, no. 11, p. 110701, 2013.
[8] K. Christensen-Jeffries, R. J. Browning, M. X. Tang, C. Dunsby, and R. J. Eckersley, "*In vivo* acoustic super-resolution and super-resolved velocity mapping using microbubbles," *IEEE Trans. Med. Imag.*, vol. 34, no. 2, pp. 433–440, Feb. 2015.
[9] O. Couture, B. Besson, G. Montaldo, M. Fink, and M. Tanter, "Microbubble ultrasound super-localization imaging (MUSLI)," in *Proc. IEEE Int. Ultrason. Symp. (IUS)*, vol. 797, Oct. 2011, pp. 1285–1287.
[10] F. Lin, S. E. Shelton, D. Espíndola, J. D. Rojas, G. Pinton, and P. A. Dayton, "3-D ultrasound localization microscopy for identifying microvascular morphology features of tumor angiogenesis at a resolution beyond the diffraction limit of conventional ultrasound," *Theranostics*, vol. 7, no. 1, pp. 196–204, 2017.
[11] J. Foiret, H. Zhang, T. Ilovitsh, L. Mahakian, S. Tam, and K. W. Ferrara, "Ultrasound localization microscopy to image and assess microvasculature in a rat kidney," *Sci. Rep.*, vol. 7, no. 1, 2017, Art. no. 13662.
[12] M. Siepmann, G. Schmitz, J. Bzyl, M. Palmowski, and F. Kiessling, "Imaging tumor vascularity by tracing single microbubbles," in *Proc. IEEE Int. Ultrason. Symp. (IUS)*, Oct. 2011, pp. 1906–1909.
[13] E. Betzig *et al.*, "Imaging intracellular fluorescent proteins at nanometer resolution," *Science*, vol. 313, no. 5793, pp. 1642–1645, 2006.
[14] M. J. Rust, M. Bates, and X. Zhuang, "Sub-diffraction-limit imaging by stochastic optical reconstruction microscopy (STORM)," *Nature Methods*, vol. 3, no. 10, pp. 793–795, 2006.
[15] A. Urban, C. Dussaux, G. Martel, C. Brunner, E. Mace, and G. Montaldo, "Real-time imaging of brain activity in freely moving rats using functional ultrasound," *Nature Methods*, vol. 12, pp. 873–878, Jul. 2015.
[16] S. B. Gay, C. L. Sistrom, C. A. Holder, and P. M. Suratt, "Breath-holding capability of adults. Implications for spiral computed tomography, fast-acquisition magnetic resonance imaging, and angiography," *Invest. Radiol.*, vol. 29, no. 9, pp. 848–851, 1994.
[17] S. R. Wilson, H.-J. Jang, T. K. Kim, H. Iijima, N. Kamiyama, and P. N. Burns, "Real-time temporal maximum-intensity-projection imaging of hepatic lesions with contrast-enhanced sonography," *Amer. J. Roentgenol.*, vol. 190, no. 3, pp. 691–695, 2008.
[18] T. Dertinger, R. Colyer, G. Iyer, S. Weiss, and J. Enderlein, "Fast, background-free, 3D super-resolution optical fluctuation imaging (SOFI)," *Proc. Nat. Acad. Sci. USA*, vol. 106, no. 52, pp. 22287–22292, 2009.
[19] A. Bar-Zion, C. Tremblay-Darveau, O. Solomon, D. Adam, and Y. C. Eldar, "Fast vascular ultrasound imaging with enhanced spatial resolution and background rejection," *IEEE Trans. Med. Imag.*, vol. 36, no. 1, pp. 169–180, Jan. 2017.
[20] A. Bar-Zion, O. Solomon, C. Tremblay-Darveau, D. Adam, and Y. C. Eldar, "Sparsity-based ultrasound super-resolution imaging," in *Proc. 23rd Eur. Symp. Ultrasound Contrast Imag.*, 2017, pp. 156–157.
[21] A. Beck and M. Teboulle, "A fast iterative shrinkage-thresholding algorithm for linear inverse problems," *SIAM J. Imag. Sci.*, vol. 2, no. 1, pp. 183–202, 2009.
[22] Z. Tan, Y. C. Eldar, A. Beck, and A. Nehorai, "Smoothing and decomposition for analysis sparse recovery," *IEEE Trans. Signal Process.*, vol. 62, no. 7, pp. 1762–1774, Apr. 2014.
[23] D. L. Donoho, "Compressed sensing," *IEEE Trans. Inf. Theory*, vol. 52, no. 4, pp. 1289–1306, Apr. 2006.
[24] Y. C. Eldar and G. Kutyniok, *Compressed Sensing: Theory and Applications*. Cambridge, U.K.: Cambridge Univ. Press, 2012.
[25] O. Solomon, M. Mutzafi, M. Segev, and Y. C. Eldar, "Sparsity-based super-resolution microscopy from correlation information," *Opt. Express*, vol. 26, no. 14, pp. 18238–18269, 2018.
[26] O. Solomon, Y. C. Eldar, M. Mutzafi, and M. Segev. (2017). "SPARCOM: Sparsity based super-resolution correlation microscopy." [Online]. Available: https://arxiv.org/abs/1707.09255
[27] Y. C. Eldar, *Sampling Theory: Beyond Bandlimited Systems*. Cambridge, U.K.: Cambridge Univ. Press, 2015.

[28] M. Elad, *Sparse and Redundant Representations: From Theory to Applications in Signal and Image Processing*. New York, NY, USA: Springer-Verlag, 2010.
[29] R. Baraniuk and P. Steeghs, "Compressive radar imaging," in *Proc. IEEE Radar Conf.*, Apr. 2007, pp. 128–133.
[30] M. Lustig, D. Donoho, and J. M. Pauly, "Sparse MRI: The application of compressed sensing for rapid MR imaging," *Magn. Reson. Med.*, vol. 58, no. 6, pp. 1182–1195, 2007.
[31] T. Chernyakova and Y. Eldar, "Fourier-domain beamforming: The path to compressed ultrasound imaging," *IEEE Trans. Ultrason., Ferroelectr., Freq. Control*, vol. 61, no. 8, pp. 1252–1267, Aug. 2014.
[32] E. Osherovich *et al.*, "Sparsity-based single-shot subwavelength coherent diffractive imaging," in *Proc. IEEE 27th Conv. Elect. Electron. Eng. Israel*, vol. 11, no. 5, 2012, pp. 1–2.
[33] P. Pal and P. P. Vaidyanathan, "Pushing the limits of sparse support recovery using correlation information," *IEEE Trans. Signal Process.*, vol. 63, no. 3, pp. 711–726, Feb. 2015.
[34] D. Cohen and Y. C. Eldar, "Sub-Nyquist sampling for power spectrum sensing in cognitive radios: A unified approach," *IEEE Trans. Signal Process.*, vol. 62, no. 15, pp. 3897–3910, Aug. 2014.
[35] C. Demené *et al.*, "Spatiotemporal clutter filtering of ultrafast ultrasound data highly increases Doppler and fUltrasound sensitivity," *IEEE Trans. Med. Imag.*, vol. 34, no. 11, pp. 2271–2285, Nov. 2015.
[36] R. J. Eckersley, C. T. Chin, and P. N. Burns, "Optimising phase and amplitude modulation schemes for imaging microbubble contrast agents at low acoustic power," *Ultrasound Med. Biol.*, vol. 31, no. 2, pp. 213–219, Feb. 2005.
[37] S. Bjærum, H. Torp, and K. Kristoffersen, "Clutter filter design for ultrasound color flow imaging," *IEEE Trans. Ultrason., Ferroelectr., Freq. Control*, vol. 49, no. 2, pp. 204–209, Feb. 2002.
[38] N. de Jong, *Acoustic Properties of Ultrasound Contrast Agents*. The Hague, The Netherlands: Cip-Gegevens Koninklijke Bibliotheek, 1993.
[39] D. H. Simpson, C. T. Chin, and P. N. Burns, "Pulse inversion Doppler: A new method for detecting nonlinear echoes from microbubble contrast agents," *IEEE Trans. Ultrason., Ferroelectr., Freq. Control*, vol. 46, no. 2, pp. 372–382, Mar. 1999.
[40] J. A. Jensen, "Estimation of blood velocities using ultrasound," in *A Signal Processing Approach*. Cambridge, U.K.: Cambridge Univ. Press, 1996.
[41] R. Cohen and Y. C. Eldar, "Sparse Doppler sensing based on nested arrays," *IEEE Trans. Ultrason., Ferroelectr., Freq. Control*, to be published.
[42] A. Bar-Zion, C. Tremblay-Darveau, M. Yin, D. Adam, and F. S. Foster, "Denoising of contrast-enhanced ultrasound cine sequences based on a multiplicative model," *IEEE Trans. Biomed. Eng.*, vol. 62, no. 8, pp. 1969–1980, Aug. 2015.
[43] C. Tremblay-Darveau *et al.*, "Improved contrast-enhanced Power Doppler using a coherence-based estimator," *IEEE Trans. Med. Imag.*, vol. 36, no. 9, pp. 1901–1911, Sep. 2017.
[44] L. I. Rudin, S. Osher, and E. Fatemi, "Nonlinear total variation based noise removal algorithms," *Phys. D, Nonlinear Phenomena*, vol. 60, nos. 1–4, pp. 259–268, 1992.
[45] A. Beck and M. Teboulle, "Fast gradient-based algorithms for constrained total variation image denoising and deblurring problems," *IEEE Trans. Image Process.*, vol. 18, no. 11, pp. 2419–2434, Nov. 2009.
[46] C. A. Schneider, W. S. Rasband, and K. W. Eliceiri, "NIH Image to ImageJ: 25 years of image analysis," *Nature*, vol. 9, no. 7, pp. 671–675, 2012.
[47] M. Ovesný, P. Křížek, J. Borkovec, Z. Švindrych, and G. M. Hagen, "ThunderSTORM: A comprehensive ImageJ plug-in for PALM and STORM data analysis and super-resolution imaging," *Bioinformatics*, vol. 30, no. 16, pp. 2389–2390, 2014.
[48] D. Ackermann, G. Schmitz, and S. Member, "Detection and tracking of multiple microbubbles in ultrasound B-mode images," *IEEE Trans. Ultrason., Ferroelectr., Freq. Control*, vol. 63, no. 1, pp. 72–82, Jan. 2016.
[49] C. Tremblay-Darveau, R. Williams, L. Milot, M. Bruce, and P. N. Burns, "Combined perfusion and Doppler imaging using plane-wave nonlinear detection and microbubble contrast agents," *IEEE Trans. Ultrason., Ferroelectr., Freq. Control*, vol. 61, no. 12, pp. 1988–2000, Dec. 2014.
[50] O. Solomon, R. J. G. van Sloun, H. Wijkstra, M. Mischi, and Y. C. Eldar. (Apr. 2018). "Exploiting flow dynamics for super-resolution in contrast-enhanced ultrasound." [Online]. Available: https://arxiv.org/abs/1804.03134

Avinoam Bar-Zion was born in Haifa, Israel. He received the B.Sc. degree *(summa cum laude)* in biomedical engineering from the Technion–Israel Institute of Technology, Haifa, Israel, in 2010, and the Ph.D. degree in 2016. During his Ph.D., he completed a year of research at Sunnybrook Hospital, Toronto, ON, Canada, as a part of a collaboration between the Technion–Israel Institute of Technology and the Medical Biophysics Department, University of Toronto, Toronto.

He is currently a Marie Skłodowska-Curie Post-Doctoral Fellow with the Shapiro Lab, Department of Chemical Engineering, California Institute of Technology, Pasadena, CA, USA. His research interests include contrast-enhanced ultrasound imaging, medical signal and image processing, synthetic biology, and computer-aided diagnosis.

Oren Solomon (S'17) received the B.Sc. degree in electrical engineering from the Ben-Gurion University of the Negev, Beersheba, Israel, in 2008, and the M.Sc. degree *(cum laude)* in electrical engineering from Tel Aviv University, Tel Aviv, Israel, in 2012. He is currently pursuing the Ph.D. degree in electrical engineering from the Technion–Israel Institute of Technology, Haifa, Israel.

His research focus is on the development of algorithmic tools for fast super-resolution imaging.

Charles Tremblay-Darveau was born in Saint-Charles-Borromée, Canada, in 1987. He received the B.Sc. degree in physics from McGill University, Montreal, QC, Canada, in 2009, and the M.S. and Ph.D. degrees in medical biophysics from the University of Toronto, Toronto, ON, Canada, in 2011 and 2015, respectively.

He was a Post-Doctoral Fellow with the Sunnybrook Research Institute, Toronto, ON, Canada. He is currently a System Designer with Philips Healthcare. His research interests include nanofluidics, Doppler contrast-enhanced ultrasound imaging, elastography, and non-invasive blood pressure measurements with microbubbles.

Dan Adam (M'64) was born in Israel. He received the B.Sc. and M.Sc. degrees in EE and the D.Sc. degree in BME from the Technion–Israel Institute of Technology, Haifa, Israel, in 1968, 1973, and 1977, respectively.

He was with Tufts University, Boston, MA, USA, from 1978 to 1980, also with the Massachusetts Institute of Technology (MIT) Cambridge, MA, USA, from 1980 to 1983, and teaching with the Harvard-MIT Health Sciences and Technology, Cambridge, MA, USA. He joined the Technion–Israel Institute of Technology in 1983, became a Full Professor in 2006, and the Dean of the Department of Biomedical Engineering from 2009 to 2012. He had a sabbatical at NIH, from 1992 to 1993. His research interests are ultrasound processing: bean-forming design, coded excitation, ultrasound RF processing, echocardiography strain imaging, including layer-specific 2-D strain measurements as a diagnostic tool of myocardial pathologies, ultrasound control of thermotherapy-monitoring of thermal-cavitational therapy, multi-modality cardiac imaging, ultrasound super-resolution imaging, perfusion measurements, and quantification of neovasculature within plaques and tumours-using contrast agents, targeted drug/gene delivery using ultrasound and micro-bubbles, non-invasive thrombolysis, cardiac pacing by non-invasive high-intensity focused ultrasound, and neural activation by non-invasive high-intensity focused ultrasound.

Dr. Adam is a fellow of European Alliance for Medical and Biological Engineering and Science, elected to IEEE-EMBS AdCom 1999, Board of Computers in Cardiology from 1990 to 1999, has been on the Board of ISMBE since 1988, its President until 2007, and its delegate to IFMBE. He has advised over 50 M.Sc. students, 16 Ph.D. students, and is currently leading a research group of six to eight graduate students (two to three Ph.D.), two to four undergraduate students, and three scientists/engineers.

Yonina C. Eldar (S'98–M'02–SM'07–F'12) received the B.Sc. degree in physics and the B.Sc. degree in electrical engineering from Tel Aviv University Tel Aviv, Israel, in 1995 and 1996, respectively, and the Ph.D. degree in electrical engineering and computer science from the Massachusetts Institute of Technology (MIT), Cambridge, MA, USA, in 2002.

She is currently a Professor with the Department of Electrical Engineering, Technion–Israel Institute of Technology, Haifa, Israel, where she holds the Edwards Chair in engineering. She is also a Visiting Professor with the Research Laboratory of Electronics, MIT, an Adjunct Professor with Duke University, Durham, NC, USA, and was a Visiting Professor with Stanford University, Stanford, CA, USA. She has authored the book *Sampling Theory: Beyond Bandlimited Systems* and co-authored the books *Compressed Sensing* and *Convex Optimization Methods in Signal Processing and Communications* (Cambridge University Press). Her research interests are in the broad areas of statistical signal processing, sampling theory and compressed sensing, optimization methods, and their applications to biology and optics.

Dr. Eldar was a member of the IEEE Signal Processing Theory and Methods and Bio Imaging Signal Processing technical committees. She was a member of the Young Israel Academy of Science and Humanities and the Israel Committee for Higher Education. She is a member of the Israel Academy of Sciences and Humanities (elected in 2017) and a EURASIP Fellow. She is a member of the IEEE Sensor Array and Multichannel Technical Committee and serves on several other IEEE committees. She was a Horev Fellow of the Leaders in Science and Technology Program at the Technion–Israel Institute of Technology and an Alon Fellow. She has received many awards for excellence in research and teaching, including the IEEE Signal Processing Society Technical Achievement Award (2013), the IEEE/AESS Fred Nathanson Memorial Radar Award (2014), and the IEEE Kiyo Tomiyasu Award (2016). She received the Michael Bruno Memorial Award from the Rothschild Foundation, the Weizmann Prize for Exact Sciences, the Wolf Foundation Krill Prize for Excellence in Scientific Research, the Henry Taub Prize for Excellence in Research (twice), the Hershel Rich Innovation Award (three times), the Award for Women with Distinguished Contributions, the Andre and Bella Meyer Lectureship, the Career Development Chair at the Technion–Israel Institute of Technology, the Muriel & David Jacknow Award for Excellence in Teaching, and the Technion's Award for Excellence in Teaching (two times). She received several best paper awards and best demo awards together with her research students and colleagues, including the SIAM Outstanding Paper Prize, the UFFC Outstanding Paper Award, the Signal Processing Society Best Paper Award, and the IET Circuits, Devices and Systems Premium Award, and was selected as one of the 50 most influential women in Israel. She is the Editor-in-Chief of *Foundations and Trends in Signal Processing*. She served as an Associate Editor for the IEEE TRANSACTIONS ON SIGNAL PROCESSING, the *EURASIP Journal of Signal Processing*, the *SIAM Journal on Matrix Analysis and Applications*, and the *SIAM Journal on Imaging Sciences*. She was a Co-Chair and a Technical Co-Chair of several international conferences and workshops. She was a Signal Processing Society Distinguished Lecturer.